A Study of the Extinction-to-Backscatter Ratio of Marine Aerosol during the Shoreline Environment Aerosol Study*

SARAH J. MASONIS, THEODORE L. ANDERSON, AND DAVID S. COVERT

Joint Institute for the Study of the Atmosphere and Ocean, University of Washington, Seattle, Washington

VLADIMIR KAPUSTIN, ANTONY D. CLARKE, STEVEN HOWELL, AND KENNETH MOORE

Department of Oceanography, University of Hawaii at Manoa, Honolulu, Hawaii

(Manuscript received 23 July 2002, in final form 20 December 2002)

ABSTRACT

Ground-based aerosol optical measurements made at near-ambient relative humidity (RH) under clean marine sampling conditions are presented and compared to 1) almost identical optical measurements made at a polluted continental site and 2) optical properties calculated from measured size distributions and Mie theory. The use of Mie theory (which assumes homogeneous spheres) is justified based on the fact that the sea-salt aerosol was measured in a hydrated state. This study focuses on the extinction-to-backscatter ratio *S*, an optical property required to interpret remote measurements by elastic backscatter lidar. For clean marine conditions, *S* is found to be 25.4 ± 3.5 sr at 532 nm (central value ± 95% confidence uncertainty). Other optical properties reported include single-scattering albedo, wavelength dependence of scattering, fraction of scattering due to submicrometer particles, and hemispheric-backscatter fraction, as well as the extensive properties (e.g., scattering coefficient) upon which these intensive properties are based. In addition, correlation scale lengths are examined via the autocorrelation function. Except during deliberate drying experiments that lowered the measurement RH below 43%, *S* exhibited little variation with RH. A subtle but clearly detectable change in optical properties was observed at the onset of volcanically influenced sampling conditions.

1. Introduction

Here we present results from in situ measurements of the lidar ratio and other aerosol optical properties from the Shoreline Environment Aerosol Study (SEAS). The campaign took place from 16 April to 1 May 2000 at Bellows Fields Air Force Base on the east side of Oahu, where the University of Hawaii (UH) Department of Oceanography maintains a tower for aerosol measurements. The tower is on the edge of a beach with a reef-induced surf zone approximately 1 km directly east, as described in the accompanying paper by Clarke and Kapustin (2003).

A goal of the SEAS project was to field test new instruments that participants hoped could be used to better characterize the chemical and radiative properties of marine aerosol. As part of this effort, participants from the University of Washington deployed equipment to measure aerosol integrated light scattering at three wavelengths (450, 550, and 700 nm), light absorption at 550 nm, and 180° backscatter at 532 nm. Integrated light scattering (σ_{sp}) was measured with a TSI, Inc., Model 3563 nephelometer, light absorption (σ_{ap}) with a Radiance Research Particle Soot Absorption Photometer (PSAP), and 180° backscatter (β_p) with a modified TSI, Inc., 3551 nephelometer (the ''180°-backscatter nephelometer''; Doherty et al. 1999). The former two instruments are routinely used for field measurements of aerosol optical properties, and their operation and data reduction procedures have established protocols (Anderson et al. 1996; Anderson and Ogren 1998; Bond et al. 1999). Previous to SEAS, however, the 180°-backscatter nephelometer—developed by our group at the University of Washington—had only been deployed for three field campaigns: prototype tests at the Cheeka Peak Observatory (CPO) on the Washington coast (Doherty et al. 1999), and measurements of pollution at Bondville, Illinois (Anderson et al. 2000), and over the Indian Ocean (Masonis et al. 2002). Other than the prototype tests at CPO, SEAS comprised the first in situ measurements of 180° backscatter in a clean marine environment and the first measurements where a significant portion of light scattering was due to supermicron aerosol (i.e., particle diameter $D > 1$ μm). The measure-

* Joint Institute for the Study of the Atmosphere and Ocean Contribution Number 916.

Corresponding author address: Dr. Sarah J. Masonis, JISAO, c/o Dept. of Atmospheric Sciences, Box 351640, Seattle, WA 98195.
E-mail: sarahd@atmos.washington.edu

ments at CPO were brief and, in contrast to SEAS, clean marine aerosol concentrations were always quite low. Because of this the CPO data are not very robust, and variability in several of the aerosol optical properties is dominated by instrumental noise.

Further, for SEAS we have compared our measured optical properties with those calculated from measured size distributions and Mie theory (section 5). These size distributions were measured by a group from UH as described in an accompanying paper by Clarke et al. (2003). Because hydrated sea-salt aerosol should be nearly spherical and because the physical and chemical properties of sea salt are relatively well understood (Tang et al. 1997), Mie theory should be quite accurate for predicting the optical properties of sea-salt aerosol. While the 180°-backscatter nephelometer was tested for accuracy using latex spheres (Anderson et al. 2000), comparison of our measurements with measured size distributions and Mie theory constitutes an independent test based on measurements of real atmospheric aerosol.

The SEAS data we present herein are the clean marine correlative to the data presented by Anderson et al. (2000) from a polluted continental site for the Lidar In-Situ Comparison (LINC) campaign in Bondville, Illinois. The measurement configuration and data processing techniques for these experiments were nearly identical, and for both LINC and SEAS there was a special focus on determining the mean, variability, and controlling factors for the aerosol extinction-to-backscatter ratio, *S*, also known as the lidar ratio. The lidar ratio is defined as

$$S \equiv \frac{\sigma_{sp} + \sigma_{ap}}{\beta_p} = \frac{\sigma_{ep}}{\beta_p}, \tag{1}$$

where σ_{ep} is total aerosol light extinction and β_p is the aerosol 180° backscatter. For all of the data presented herein, *S* was derived for 532-nm wavelength light. We are interested in measuring the lidar ratio because knowledge of *S* allows for the inversion of elastically backscattered lidar signals for aerosol light extinction versus range. If the aerosol extinction-to-backscatter ratio is not known, then either an assumed value of *S* must be used in the lidar retrieval—leading to very large uncertainties in light extinction—or more sophisticated measurement methods, such as the slant-path method (Reagan et al. 1977; Spinhirne et al. 1980), high-spectral-resolution lidar (Shipley et al. 1983; Sroga et al. 1983; Grund and Eloranta 1991; Piironen and Eloranta 1994), or Raman lidar (Ansmann et al. 1990, 1992; Ferrare et al., 1998a,b; Mattis et al. 2002), must be used. However, most lidar instruments are not equipped to employ these techniques and so rely on a priori knowledge of *S* for physically meaningful retrievals.

Of interest is how *S* varies with the aerosol single-scatter albedo (ω), the Ångström exponent ($\mathring{a}$), and the fine-mode fraction of light scattering (FMF_{scat}). These parameters are derived from aerosol light scattering (σ_{sp}) and light absorption (σ_{ap}) as follows:

$$\omega \equiv \frac{\sigma_{sp}}{\sigma_{sp} + \sigma_{ap}} = \frac{\sigma_{sp}}{\sigma_{ep}}, \tag{2}$$

$$\mathring{a}\left(\frac{\lambda_1}{\lambda_2}\right) \equiv -\log\left(\frac{\sigma_{sp,\lambda_1}}{\sigma_{sp,\lambda_2}}\right) \Big/ \log\left(\frac{\lambda_1}{\lambda_2}\right), \quad \text{and} \tag{3}$$

$$FMF_{scat} \equiv \frac{\sigma_{sp,D<1\,\mu m}}{\sigma_{sp,D<10\,\mu m}}, \tag{4}$$

where $\sigma_{sp,D<1\mu m}$ is light scattered only by aerosol of aerodynamic diameter $D_{aero} < 1$ μm, and $\sigma_{sp,D<10\mu m}$ is σ_{sp} due to all aerosol with $D_{aero} < 10$ μm. Covariance between *S* and these parameters is of interest because ω, $\mathring{a}$, and FMF_{scat} are indicators of aerosol type and may provide some predictive capacity for *S*.

Because lidar instruments measure ambient aerosol, and because *S* is expected to vary with aerosol hydration, it is important that we measure *S* at near-ambient relative humidity. Since there is only one 180°-backscatter nephelometer in existence at this time, we chose to try and measure β_p at as close to ambient RH as possible. Thus our experiment was configured to keep the instruments at near-ambient air temperature.

The sampling configurations and protocols used for LINC and SEAS provide the information on the sampled aerosol and on instrument performance needed to report not only the mean aerosol optical parameters but also the uncertainty of the mean values and their variability on short (minutes) and long (days to weeks) timescales. It is important that we know both the accuracy of the in situ measurements so that we understand how well we have determined mean values and so that we can distinguish whether aerosol optical parameters such as the lidar ratio are distinctly different for different types of aerosol. If the in situ measurements are to be of use to lidar applications, it is also important that we know how much *S* changes with time and/or distance, both for a given location and for a given airmass type.

2. Aerosol sampling configuration

The SEAS campaign took place at a site on the Bellows Field Air Force Base that is maintained by the UH Department of Oceanography. A key feature of this site is that it is located on the beach and, when there are east–northeast trade winds, it is directly downwind of an offshore reef (Clarke and Kapustin 2003). Aerosol reaching the site under these conditions is a combination of remote marine aerosol and aerosol from the wave break at the reef. A second feature of the site is a tower that UH built so that aerosol can be measured at various altitudes above sea level, as there is expected to be a significant vertical gradient in both aerosol concentration and temporal variability.

During the SEAS campaign our instruments were

housed in a shed tied down to a scaffolding platform on the tower at ~6 m elevation. Our sample air was drawn through an inlet mounted on the scaffolding tower at ~11 m altitude. The inlet used for most of the campaign was a tapered tube with an inverted bowl-shaped cover of ~30 cm diameter, so that wind direction did not affect the inlet passing efficiency. Several other inlet configurations were tested for losses using an aerodynamic particle sizer (APS) by alternately measuring the aerosol size distribution with each inlet in place. Alternate inlets included a standard diffuser with a tip velocity of 8 m s^{-1} and a simple tube with a tip velocity of 2 m s^{-1}. Both were pointed manually into the prevailing 5–10 m s^{-1} wind. An APS was also used to check for losses in our system plumbing. The aerosol volume distribution was centered on ~3.6 μm diameter, and in all cases aerosol volume went to zero by ~9 μm. Measurement from up- and downstream of our inlets and sample lines indicated significant losses above ~7 μm aerodynamic diameter, and it is unlikely that particles larger than 10 μm, if present, were sampled. Therefore, the results herein apply to sub-10-μm aerosol only.

Aerosols drawn through the inlet were routed through a hole in the shed wall to the optical instruments. In an effort to keep the instruments at near-ambient temperature the shed was protected from rain and sunlight with a white tarp and was heavily ventilated with ambient air. The most significant source of heat in the shed was the lamp light source in the integrating nephelometer. To mitigate heating, we removed the lamp cover, reduced its power from the usual 75 to 40 W, and blew air across the lamp.

Instrument calibration and noise levels were monitored via periodic gas calibrations and twice-daily, automated filtered air measurements. The coarse-mode component of the aerosol was also determined by cycling between measuring the components of light scattering and absorption due to all aerosol of aerodynamic diameter $D_{aero} < 10$ μm and that due to aerosol with $D_{aero} < 1$ μm. The sub-1- and sub-10-μm aerosol were alternately measured for 10-min intervals 3 times in a row at intervals of about 4 h. These data are used to calculate the fine-mode fraction of light scattering, FMF_{scat}.

For the data shown herein, the wind direction was always such that we were sampling marine air. As one would expect for a near-surface marine site, the ambient relative humidity during SEAS was never very low (54% RH minimum). We were interested in measuring how the lidar ratio of sea salt changes with RH, so we intentionally lowered the sample RH several times. This was done by either heating the sample or by diluting it with dry air; the data shown here are all from heating runs.

3. Data reduction

We have described the instruments used to determine light scattering, light absorption, and 180° backscatter. However, the quantities measured by the in situ instruments are not exactly the desired parameters. In each case we must adjust or correct the measured value in order to get σ_{sp}, σ_{ap}, or β_p. Note that the lidar ratio is calculated using values of σ_{sp} and β_p at a common relative humidity, but these parameters are never *measured* at the same RH because of different amounts of heating in the instruments. Because we do not know how β_p changes with RH,[1] σ_{sp}, β_p, and S are derived at the RH measured by 180°-backscatter nephelometer.

All data herein are referenced to ambient air density. The nephelometers were calibrated with air and CO_2 periodically throughout the campaign, and we routinely measured filtered air with the nephelometers and PSAP as a zero check and noise measurement.

a. Integrating nephelometer data processing

The integrating nephelometer senses light scattering at three wavelengths (450, 550, and 700 nm). The measured quantities correspond closely to total scatter at the three wavelengths but are not exactly σ_{sp} because of imperfections in the measurement method. The reported values of light scattering were adjusted for variations in each detection channel's calibration slope and offset (see Anderson and Ogren 1998) and for angular nonidealities in the integrating nephelometer. Angular nonidealities exist because the instrument's light source is non-Lambertian, and the nephelometer only measures light scattered into the angles 7°–170° (total scattering) and 90°–170° (hemispheric backscattering). The magnitude of the angular correction factor varies with aerosol size and is significant (30%–50% of total scattering) for coarse-mode-dominated aerosol such as that measured during SEAS. A correction algorithm described by Anderson and Ogren (1998) uses the Ångström exponent to estimate the appropriate angular correction factor. However, these correction factors are based on a suite of simulations that cover a large range of aerosol sizes and indices of refraction. During SEAS, the University of Hawaii measured the size distribution of the aerosol from the same location on the tower at which we were making our optical measurements (i.e., their tower location ''t2''; Clarke et al. 2003). Thus, we used these size distributions and an index of refraction of $m = 1.40 + 0.00i$ for the coarse mode and $m = 1.400 + 0.005i$ (clean marine) or $m = 1.400 + 0.009i$ (volcanically influenced) for the accumulation mode to generate angular correction factors specific to the aerosol measured during SEAS. (See section 5 for how these values of m were selected.) Mie theory was used to calculate the ratio of true total (0°–180° Lambertian illumination) scattering to the nephelometer-measured

[1] While we did do tests where we lowered the sample volume RH to see how S changes with humidity, the limited data do not allow separation of RH effects from temporal changes in concentration for extensive parameters like β_p.

scattering. The resulting angular correction factor was about 22% higher than that given by the ''no cut'' formulas in Table 4b of Anderson and Ogren (1998).

After angular correction, the derived values of $\sigma_{sp,\lambda 1}$ and $\sigma_{sp,\lambda 2}$ were used to calculate the Ångström exponent. These are the values of $\mathring{a}$ that we present herein.

Scattering values were also adjusted from instrument to ambient air density and from the integrating nephelometer RH to the 180°-backscatter nephelometer RH. When the sample air is not subject to intentional RH control, the relative humidity in the integrating nephelometer is almost always lower than that of the 180°-backscatter nephelometer because the lamp in the integrating nephelometer heats the sample air much more than does the laser light source. The adjustment was therefore usually in the positive direction and it was usually small (<10% of σ_{sp}).

Light scattering generally increases nonlinearly with hygroscopic growth (Covert et al. 1972), and a reasonable fit to σ_{sp} versus RH is given by $f(\mathrm{RH})$, where

$$f(\mathrm{RH}) = \left(\frac{100 - \mathrm{RH}_{meas}}{100 - \mathrm{RH}_{180}}\right)^{\gamma} \quad (5)$$

such that

$$\sigma_{sp,RH180} \approx \sigma_{sp,meas} f(\mathrm{RH}). \quad (6)$$

Here $\sigma_{sp,RH180}$ is light scattering at the 180°-backscatter nephelometer RH (RH_{180}), RH_{meas} is the integrating nephelometer RH, and γ is a function of the aerosol type (Carrico et al. 1998 and 2000; Kotchenruther et al. 1999; Gasso et al. 2000). The only cases in which Eq. (5) does not provide a good approximation of σ_{sp} versus RH are those in which the sample aerosol has a deliquescence or crystallization point and we are near that point. Sea-salt, the dominant aerosol during SEAS, has deliquescence and crystallization points at ~70%–75% RH and ~43% RH, respectively (Tang et al. 1997). For the SEAS measurements, the ambient aerosol should always be hydrated since it is sampled near the level of the ocean surface; indeed, the ambient RH outside of our instrument shed was always greater than 54%. Heating of the sampled air lowers the RH slightly, but the RH in the integrating nephelometer (the warmest location in our sample stream) did not drop below 50%—and was usually >60%—under normal sampling conditions. Thus, the measured aerosol should always have been in a hydrated state. The exception was when we deliberately ran drying tests, which showed evidence of changed aerosol optical properties consistent with crystallization.

For this campaign we did not employ scanning RH measurements sufficient to determine γ empirically. Therefore, we adopt a value of $\gamma = 0.65$, consistent with the measured size distributions and laboratory studies of sea-salt hydration by Tang et al. (1997). This value is also consistent with empirical measurements of σ_{sp} versus RH made at clean marine sites (Carrico et al. 1998; Gasso et al. 2000).

Finally, the 10-s average values of σ_{sp} at 550 nm were adjusted to 532 nm using

$$\sigma_{sp,532nm} = \sigma_{sp,550nm}(550\ \mathrm{nm}/532\ \mathrm{nm})^{\mathring{a}(450,550)}. \quad (7)$$

b. 180°-backscatter nephelometer data processing

As with the integrating nephelometer data, the 180°-backscatter nephelometer data must be adjusted from instrument to ambient air density and be corrected for changes in the instrument calibration. Variations in the calibration coefficients had a random, noiselike quality. The magnitude of the change between gas calibrations was not related to the elapsed time between the calibrations, even when multiple calibrations were run in rapid succession. Because variations in the calibration appear to be noiselike—rather than due to a drift in the instrument sensitivity or wall scatter—the optimal calibration coefficients should be given by the ensemble of calibrations. A single set of calibration coefficients was therefore used for all 180°-backscatter data, as long as the system was not realigned. It was necessary to realign the system once during SEAS, so we use one pair of values before the alignment and a new pair after the alignment.

The 180°-backscatter nephelometer does not actually measure 180° backscatter but instead measures integrated ~176°–178° scattering. The conversion from this flux quantity to the radiance quantity β_p is incorporated into the calibration, and for most aerosol $\sigma_{176°–178°}$ is an excellent approximation for β_p (Doherty et al. 1999). However, for large ($D > 1\ \mu$m) homogeneous spheres Mie theory predicts a significant difference between the two quantities because of resonance in the scattered wave fronts (Fig. 1). Hydrated sea-salt aerosol fits this description, so for cases where our measurement RH exceeded 50%, we adjusted the 180°-backscatter nephelometer measurements using a correction factor that is derived from Mie theory. The same model input was used here as was used to determine the angular correction factors for the integrating nephelometer data. This approach yields a multiplicative correction factor of ~1.40 for the SEAS aerosol.

This correction factor is quite large because the phase function of light scattering is highly variable at angles near 180° (Fig. 1). If the aerosol measured during SEAS is not actually spherical, this correction factor may be significantly in error. In previous studies under clean marine conditions, attempts to reach closure between nephelometer-measured light scattering and scattering derived from size distributions and Mie theory have failed for comparisons of hemispheric backscatter σ_{bsp}, even when closure was achieved for total scatter σ_{sp} (Quinn et al. 1995, 1996). In each case, the light-scattering measurements were made at low RH—below the crystallization point of sea salt—so it is likely that the

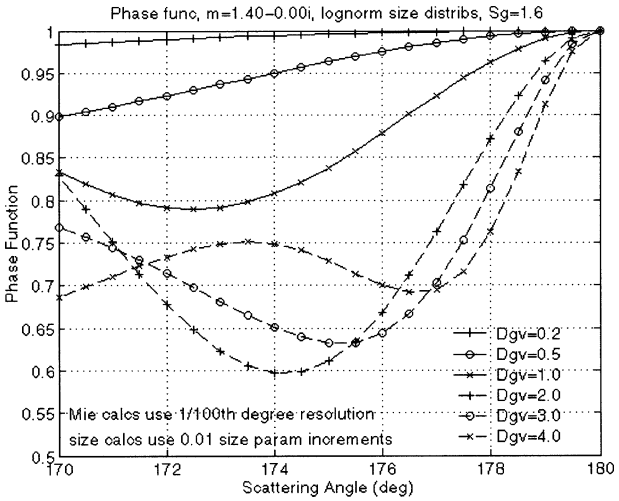

FIG. 1. Scattering phase functions near 180° for lognormal size distributions with geometric std devs of 1.6 and various geometric volume mean diameters, D_{gv}. Each phase function has been normalized to unity at 180°. Calculations assume homogeneous spheres with a refractive index of $m = 1.400 + 0.000i$. For reference, the 180°-backscatter nephelometer senses scattering between 176° and 178°.

lack of closure was attributable to the fact that they were trying to simulate nonspherical aerosol using Mie theory. [It is unlikely that the nephelometer measurements were in error, because the angular correction to hemispheric backscatter is less than ~5% and the nephelometer has been shown in laboratory measurements of spherical aerosol to accurately measure hemispheric backscatter (Anderson et al. 1996).] In contrast to the previous studies of sea-salt-dominated marine aerosol at low RH, our measurements of hemispheric-backscatter fraction at near-ambient RH agree within the measurement uncertainties with Mie-calculated values that are based on measured size distributions (section 5). Thus, it seems reasonable that the homogeneous spherical model is appropriate for the SEAS aerosol and, in turn, that the 180°-backscatter correction factor (to convert $\sigma_{sp176°–178°}$ to β_p) can also be accurately calculated from Mie theory.

c. Light absorption photometer data processing

The values of σ_{ap} reported by the PSAP were corrected for inaccuracies in the flow rate, filter spot size, instrument calibration bias, and scattering enhancement of the signal using the formulations of Bond et al. (1999). Built into these corrections is an adjustment from the measured wavelength of ~565 to 550 nm. Light absorption was also adjusted from STP to ambient air density, to match the concentration for the reported values of σ_{sp} and β_p. Finally, σ_{ap} was extrapolated from 550 to 532 nm by scaling by the two wavelengths:

$$\sigma_{ap,532} = \sigma_{ap,550}(550/532). \quad (8)$$

The wavelength dependence of light absorption is not well understood. However, Eq. (8) is consistent with theoretical and field studies (Foot and Kilsby 1989). Note that the dependence of σ_{ap} on RH is also unknown, so we have not applied any RH adjustment to σ_{ap}.

The correction to σ_{ap} for scattering enhancement of the PSAP signal given by Bond et al. is a function of low-RH (45%) nephelometer scattering (i.e., preangular correction) at 550 nm. Because we do not have a direct measure of low-RH light scattering, $\sigma_{sp,dry}$ was derived from $\sigma_{sp,meas}$ using a calculation analogous to that in Eqs. (5) and (6).

d. Uncertainty analysis

Each of the adjustments to σ_{sp}, σ_{ap}, and β_p just described are potentially in error. Also, no instrument is perfectly accurate or has infinite precision. In order to constrain in situ measurements these sources of uncertainty in the derived parameters must be quantified so that 1) we can distinguish between measurement noise and true variability and 2) the concomitant uncertainty in radiative forcing can be determined.

For each extensive parameter the total uncertainty was calculated by adding the various components of uncertainty in quadrature. Inherent in this approach is an assumption that the components of uncertainty are not correlated and that each is randomly and normally distributed. Empirical data from laboratory and field measurements show that this is true for the components of uncertainty that are due to instrument noise and instrument calibration. However, it may not be true for other sources of uncertainty, especially within a given airmass type. For example, if a large number of aerosol types is sampled, it is likely that the aerosol hygroscopicity will be overestimated about as often as it will be underestimated, but for a given aerosol type it may be consistently either over- or underestimated.

We have not included in our analysis the uncertainties that are due to inlet passing efficiencies because this source of uncertainty was not carefully quantified. The derived values of σ_{sp} have six components of uncertainty, several of which were quantified by Anderson et al. (1996) and Anderson and Ogren (1998), and we employ their results directly. The uncertainties in σ_{sp} given here stem from uncertainty in nephelometer accuracy (7% of σ_{sp}; Anderson et al. 1996), instrument calibration variations and noise (Anderson and Ogren 1998), uncertainty in the angular correction factor, uncertainty in the adjustment from the measurement RH to the 180°-backscatter nephelometer RH (calculated by allowing γ to vary randomly by ± 0.2), and uncertainty in the adjustment from 550 to 532 nm (set to half the applied adjustment). As described earlier, we used measured size distributions and Mie theory to determine the angular correction factor for the integrating nephelometer. The uncertainty in this correction factor was calculated as twice the standard deviation of the range of correction factors given by varying the mean aerosol diameter of

TABLE 1. Campaign-wide statistics from the SEAS project (16 Apr–1 May 2000) are shown in columns 1–6, for only those data where the 180°-backscatter nephelometer RH (RH_{180}) was >50%. All aerosol optical properties were derived at RH_{180} and are given at 532 nm. The coefficient of variation (COV) is the std dev of a parameter divided by its mean. Because the measured std dev (SD_{meas}) includes instrumental noise, SD_{mean}/mean is an upper bound on the parameter's coefficient of variation. Here we give the average upper bound on the COV over 10 min, which corresponds to an advection length of ~3 km for a typical 5 m s^{-1} surface wind speed. For comparison, the COV for the aerosol measured during the LINC project (28 Aug–29 Sep 1999; Anderson et al. 2000) at a rural, polluted, continental site, is shown in column 7.

	Avg	Avg uncertainty in 10-min values	Avg std dev of 1-min values over 10 min	Upper bound on COV over ~3 km	Std dev of all 10-min averages	Upper bound, COV, all SEAS data	Upper bound, COV, all LINC data
RH_{180}	67.6	—	0.8	—	5.4	8%	
σ_{sp} $(Mm)^{-1}$	38.14	3.92	2.14	6%	10.41	27%	111%
σ_{ap} $(Mm)^{-1}$	0.24	0.55	0.87	363%	0.39	163%	69%
β_p $(Mm\ sr)^{-1}$	1.51	0.19	0.12	8%	0.42	28%	81%
$\mathring{a}$ (450, 700)	0.07	0.46	0.10	—	0.14	—	—
ω	0.99	0.02	0.05	5%	0.016	2%	9%
S (sr)	25.7	4.39	1.75	7%	3.71	14%	31%
FMF_{scat}	0.154	—	—	—	0.044	23%	73%

the coarse mode by ~0.3 μm around its central value. (See section 5 for a more extensive discussion of the SEAS size distributions.) This yielded uncertainties of ~7% of σ_{sp}. For coarse-mode-dominated aerosol, such as that measured during SEAS, instrument accuracy and the angular correction factor are the largest sources of uncertainty in scattering.

The components of uncertainty for the 180°-backscatter nephelometer data are instrument accuracy (7% of β_p; Anderson et al. 2000), instrument calibration variations, instrumental noise, and uncertainty in the angular correction factor that accounts for the difference between the measured 176°–178° scatter and 180° backscatter. We have noted that the ensemble of all gas calibrations was used to determine a single set of calibration coefficients for the 180°-backscatter nephelometer, as long as the system was not realigned. The variation (2 times the standard deviation) of the calibration coefficients across ensemble members is used to calculate uncertainty in the instrument calibration, resulting in an uncertainty of ~20% of β_p. Noise uncertainty is calculated using the formulation of Anderson and Ogren (1998), where σ_{sp} is replaced by β_p. This source of uncertainty is only significant when the signal becomes very small. The angular correction factor uncertainty for β_p is calculated in a manner analogous to that for the total scatter angular correction factor uncertainty, producing an uncertainty of ~7% for β_p.

For the values of $\sigma_{ap,532nm}$ derived herein, there are five components of uncertainty, the first four of which were determined by Bond et al. (1999) and are described in detail therein: instrument accuracy (20%), instrument precision (6%), instrument noise, uncertainty in the scattering correction to σ_{ap}, and uncertainty in the adjustment from σ_{ap} at 550 nm to σ_{ap} at 532 nm. The latter is set to the full value of the applied adjustment. At low levels of light absorption the uncertainty in σ_{ap} is dominated by instrument noise, and at high levels of light absorption the uncertainty is dominated by instrument accuracy uncertainty.

We calculate the uncertainty in the intensive parameters (single-scatter albedo, Ångström exponent, fine-mode fraction, and the lidar ratio) by taking the derivative of the equation used to calculate them with respect to each of its controlling parameters, then summing the product of each derivative with the uncertainty of the controlling parameter. For example, for single-scatter albedo, which is determined by σ_{sp} and σ_{ap}, the uncertainty is

$$\delta\omega = \sqrt{\left(\frac{\partial\omega}{\partial\sigma_{sp}}\delta\sigma_{sp}\right)^2 + \left(\frac{\partial\omega}{\partial\sigma_{ap}}\delta\sigma_{ap}\right)^2}. \quad (9)$$

This results in the following formulations:

$$\delta\omega = \sqrt{\left[\left(\frac{\sigma_{ap}}{\sigma_{ep}^2}\right)\delta\sigma_{sp}\right]^2 + \left[\left(\frac{\sigma_{sp}}{\sigma_{ep}^2}\delta\sigma_{ap}\right)\right]^2}, \quad (10)$$

$$\delta\mathring{a}(\lambda_1, \lambda_2) = \frac{\sqrt{\left(\frac{\delta\sigma_{sp,\lambda_1}}{\sigma_{sp,\lambda_1}}\right)^2 + \left(\frac{\delta\sigma_{sp,\lambda_2}}{\sigma_{sp,\lambda_2}}\right)^2}}{\ln\left(\frac{\lambda_1}{\lambda_2}\right)}, \quad (11)$$

$$\delta S = \sqrt{\left[\left(\frac{1}{\beta_p}\right)\delta\sigma_{sp}\right]^2 + \left[\left(\frac{1}{\beta_p}\right)\delta\sigma_{ap}\right]^2 + \left[\left(\frac{\sigma_{sp}+\sigma_{ap}}{\beta_p^2}\right)\delta\beta_p\right]^2}. \quad (12)$$

4. Results

a. Mean and variability of aerosol optical properties

The entire SEAS campaign was dominated by sea-salt aerosol, as reflected in the consistently low Ångström exponent, high single-scatter albedo, and low fine-mode fraction (Table 1, Fig. 2). Note that the average single-

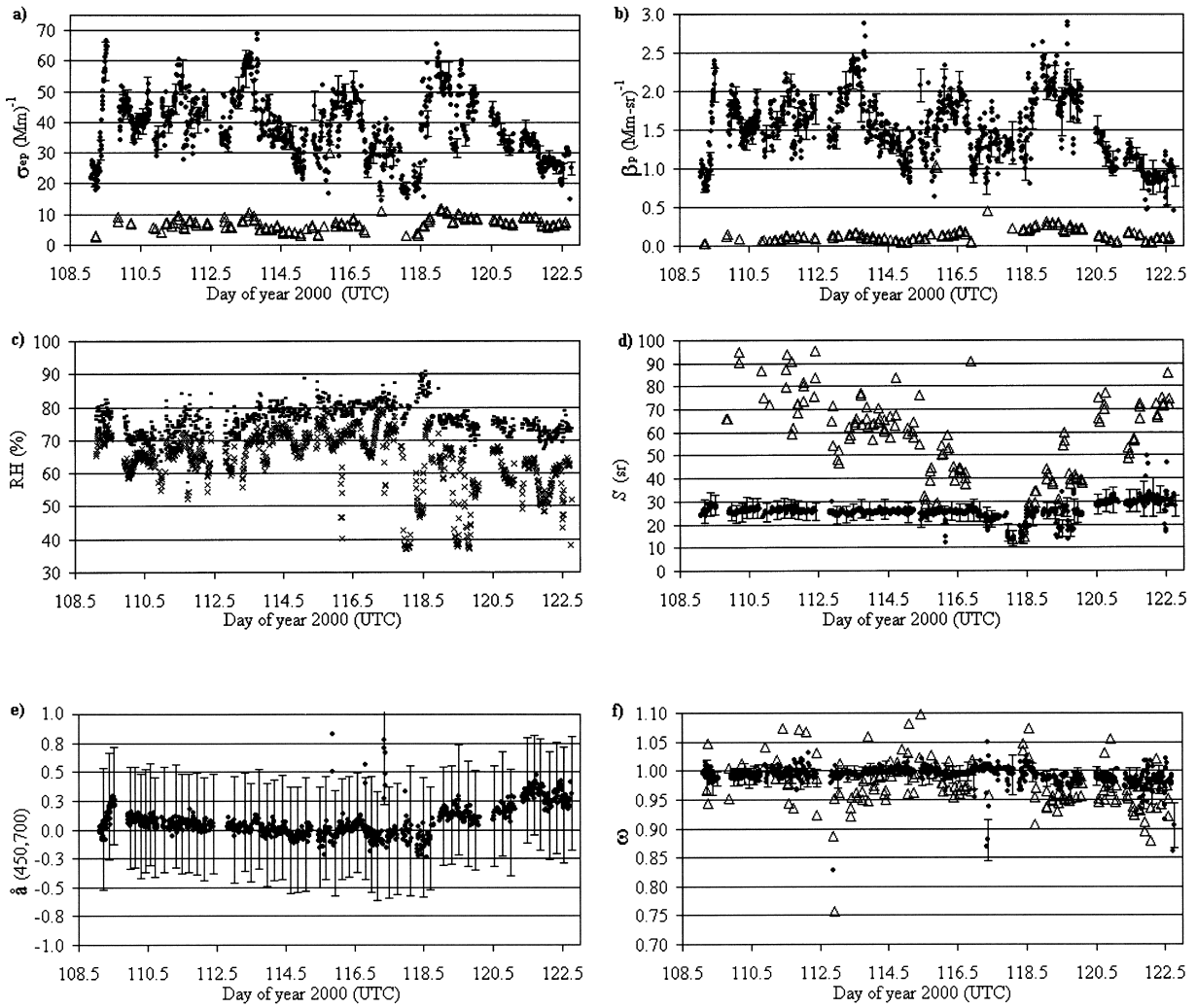

FIG. 2. SEAS campaign 10-min average values of (a) light extinction, (b) 180° backscatter, (c) RH of the air at the sampling stack inlet (dots) and of the derived light scattering parameters (crosses), (d) the lidar ratio, (e) the 450 nm:700 nm Ångström exponent, and (f) single-scatter albedo. For the optical parameters, data are shown for aerosol of geometric diameter $D < \sim 10$ μm (dots) and $D < 0.82$ μm (triangles). The $D < 10$ μm data are shown with 95% CI uncertainty bars. All optical values are at 532 nm and 180°-backscatter nephelometer RH, as given in (c) (crosses).

scatter albedo was not greater than 1 (Table 1),[2] indicating that the Bond et al. (1999) 2% scattering correction to the measured PSAP absorption is not too large. Given that σ_{sp} is almost two orders of magnitude larger than σ_{ap}, this is a fairly rigorous test. We point this out because there has been some question as to the validity of the Bond et al. scattering correction to absorption for coarse-mode aerosol. Of course, for the scattering correction to be valid, plumbing losses in the PSAP must not significantly exceed those in the nephelometer, and for this reason we used a low flow rate in the PSAP (1 L min^{-1}). Also, the 2% scattering correction was done using nephelometer-measured light-scattering values that had not yet had the angular correction factor applied, as recommended by Bond et al.

Despite the consistent aerosol composition, light extinction showed wide fluctuations, between ~15 and ~55 Mm^{-1}. As was the case for polluted aerosol we measured in Bondville (Anderson et al. 2000), most of the variation in σ_{ep} occurred at timescales longer than 10 min. During most of the experiment (18–28 April) there were strong to moderate trade winds out of the east to northeast, so the measured aerosol should have been comprised of sea salt from the open ocean, from the breaking waves at the offshore reef, and from waves breaking along the shore-

[2] The short-term variations in ω shown in Fig. 1f are dominated by instrumental noise in the measurement of σ_{ap} rather than by real atmospheric variability. Because σ_{ap} is nearly zero, the addition of noise results in both positive and negative excursions in σ_{ap}, the latter of which here yield values of σ_{ap} below zero and thus values of $\omega > 1.0$. Time averaging reduces the influence of noise, resulting in physically meaningful values of ω that are less than 1.0.

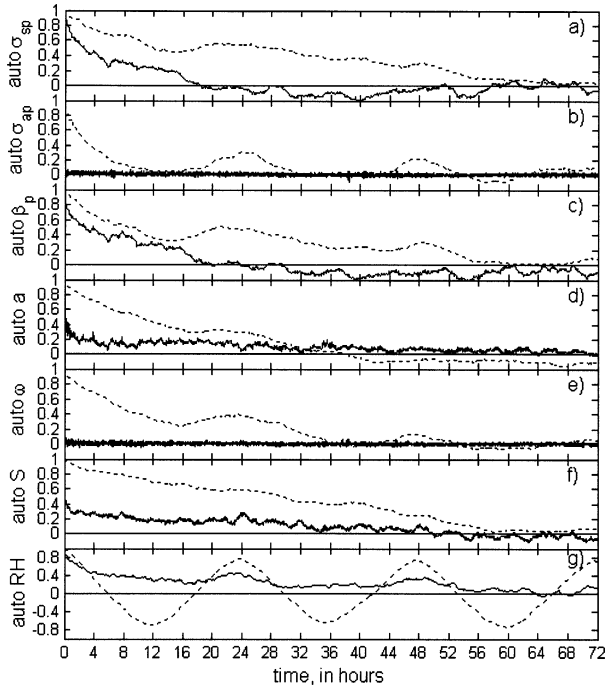

FIG. 3. Autocorrelations for (a) light scattering, (b) light absorption, (c) 180° backscatter, (d) the Ångström exponent, (e) single-scatter albedo, (f) the lidar ratio, and (g) the RH of the 180°-backscatter nephelometer, calculated from the 1-min-resolution data from the SEAS (solid lines) and LINC (dashed lines) campaigns.

line. Clarke and Kapustin (2003) show that changing tide height, wind speed, and wind direction do affect light scattering at the Bellows site. However, simple correlations do not exist between any of these factors and σ_{sp}, and not a single one of them was a dominant controlling factor during this campaign. The fact that σ_{sp} is not well correlated with tide height indicates that the aerosol was not dominated by the breaking waves at the reef, which were strongly modulated by the tide height. Further, Clarke et al. (2003) show that only about 10% of the light scattering at the altitude of our inlet (their ''t2'' inlet) was attributable to nearshore breaking waves.

All of the optical parameters showed less day-to-day variability during SEAS than for the polluted continental aerosol measured during the LINC project (Anderson et al. 2000). The timescale and nature of the measured variability is revealed by autocorrelation functions, which, for comparison, we show here for both the LINC and the SEAS data (Fig. 3). The autocorrelation function describes the ''memory'' of a parameter across a range of timescales by describing how much of a parameter's total variation occurs between time t and $t + \Delta t$. For a data series of length N the autocorrelation function is given by

$$\sum_{t=0}^{N-\Delta t} \frac{[x(t) - \bar{x}][x(t + \Delta t) - \bar{x}]}{[x(t) - \bar{x}]^2}, \qquad (13)$$

where the overbar indicates averaging. Note that the temporal autocorrelation lengths shown in Fig. 3 are related to spatial autocorrelation lengths by the average wind speed, so we can equally infer from these data the temporal or spatial scales of variability. Knowledge of these scales of variability is important for proper coordination of disparate measurements, and it can provide insight as to the physical processes driving the variations.

For SEAS, the autocorrelation functions for the light-scattering parameters drop off so rapidly that any other measurements we wish to correlate with variations in σ_{sp} or β_p should be coordinated with the optical data to within ~20 min to achieve a correlation of better than 0.9. Fully half of the variability in σ_{sp} and β_p is contained in timescales of less than 3 h. Relative humidity at the site did have a slight diurnal cycle, but neither this nor the ~11 h tide cycle are reflected in the scattering autocorrelation function. Variability in all of the optical parameters other than σ_{sp} and β_p has a strong white noise characteristic. In the case of σ_{ap} and ω this is due to the fact that the measured variability is dominated by instrumental noise. Both $\mathring{a}$ and S were also so constant across the campaign that about one-third ($\mathring{a}$) and one-half (S) of the variability were attributable to instrumental noise, and the variability that could be measured did not appear to be driven by any cyclical pattern, such as diurnal (RH) or tide height changes.

In comparison, the autocorrelation functions for the optical properties of the polluted continental aerosol at Bondville drop off quite slowly. This is consistent with the idea that most of the variation in σ_{sp} and β_p was due to longer-term changes in aerosol loading, as described by Anderson et al. (2000). Variations in σ_{ap} were at somewhat shorter timescales, and to the extent that σ_{ap} did have longer-term variations they appear to follow a diurnal cycle. A diurnal cycle is also apparent in β_p and ω but was responsible for a much smaller portion of the variability in σ_{sp} and $\mathring{a}$(450 and 700), and it appears to have had no influence on S. This is interesting because we would expect that some of the variability in the extensive properties would be related to changes in relative humidity, which itself had a strong diurnal cycle (Fig. 3g). However, we measured σ_{ap} at low RH, so the RH effect should have been strongest for σ_{sp} and β_p. The fact that it was not indicates that factors other than RH strongly influenced the variations in light scattering (σ_{sp} in particular). Also, some other type of diurnally dependent influence—such as local diesel-powered vehicles, as proposed by Anderson et al. (2000)—must have driven the variations in σ_{ap}.

b. Analysis of categorized data

One of the reasons the aerosol optical properties were not very variable during SEAS is that the local meteorology was quite consistent throughout the campaign, with the winds steady (7.0 ± 1.2 m s^{-1}) and always from offshore ($72° \pm 8°$ east of north). However, as shown by Clarke and Kapustin (2003), back trajectories indicate

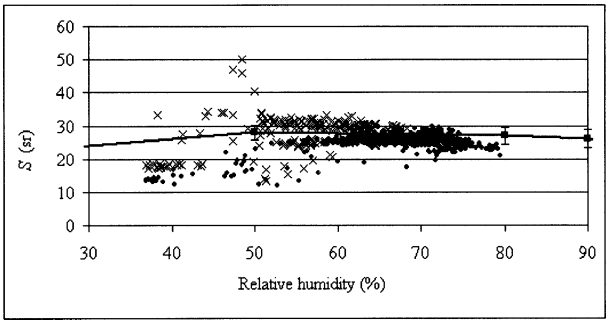

FIG. 4. Lidar ratio vs the RH at which it is derived, for all SEAS 10-min averages where we were sampling all aerosol of diameter $D < 10$ μm. Data classified as clean marine (i.e., before yearday 119.0 UTC) are shown as crosses and those classified as volcanically influenced (i.e., after yearday 119.0 UTC) are shown as dots. Also shown is (solid line and squares) S vs RH for sea-salt aerosol, as calculated by Ackermann (1998) in a theoretical study.

that there was a change in the longer-term (~5–7 day) airmass history late in yearday 118 (27 April) that was associated with a frontal passage. Before this time, trajectories for the sampled air were confined to the open Pacific Ocean; from yearday 119 to 123 UTC the trajectories passed over Japan near the active volcano Mt. Usu before crossing the Pacific to Oahu. This shift in airmass region of origin corresponded to a shift in the Ångström exponent and a more subtle change in single-scatter albedo. Accordingly, data from before and after this date have been separately analyzed. We have also separately analyzed data from when we were measuring at near-ambient RH (RH > 50%) versus from when we were intentionally lowering the sample RH (RH < 50%).

Because of the high winds and marine environment, relative humidity at the Bellows Fields site was moderate to high (~70%–90%) for the entire campaign, and only a small part of its variability was linked to a diurnal cycle (Figs. 2c, 3g). The relative humidity in the instruments was generally lower than the ambient RH by ~10%–15% (Fig. 2c). When the difference between the ambient RH and the 180°-backscatter nephelometer RH is more than ~15%, it is because we were intentionally drying the sample air (Fig. 4). What we found was that the lidar ratio was low and extremely consistent, as long as the sample relative humidity was greater than ~50%; within this regime S appeared to be independent of RH (Table 2, Fig. 4). This lack of RH dependence above 50% RH was consistent with the theoretical values of S versus RH calculated by Ackermann (1998). In contrast, our measured values of S dropped dramatically with relative humidity below ~50%, and this drop was not captured by Ackermann. This sudden transition is almost certainly caused by crystallization of the aerosol, which is known to occur between 40% and 50% RH for sea salt (Tang et al. 1997). Interestingly, in a study trying to simulate dustlike aerosol, Mishchenko et al. (1997) predicted that the lidar ratio of nonspherical aerosol is 2–2.5 times *higher* than that for spherical aerosol of the same size. However, these results were from modeling studies using an absorbing aerosol ($m = 1.5 + 0.008i$) and for a large range of coarse-mode size distributions.

Table 3 shows that lidar ratios were considerably higher for the submicron portion of the aerosol—72 sr before yearday 118.9 and 91 sr after yearday 118.9 UTC (Table 3). Unfortunately, the scattering signal was quite small for the submicron aerosol, so S was both highly variable and highly uncertain. However, inspection of time series (not shown) reveals that S was consistently higher for the fine mode than for the total aerosol when we switched between sampling $D_{\text{aero}} < 10$ μm and $D_{\text{aero}} < 1$ μm, so we believe the observed difference is not an artifact.

Direct chemical measurements of the sub- and supermicron aerosols were not made during SEAS. However, we can infer that the submicron aerosol was not dominated by pollution from the fact that the single-scatter albedo for the clean marine case was 0.98. Given the source region, it was most likely sea salt, biogenic sulfate (such as from dimethyl sulfide), or a combination of the two. After yearday 118.9, ω of the submicron aerosol dropped to 0.96, consistent with the addition of volcanic aerosol.

The aerosol intensive parameters (ω, $\mathring{a}$, and S) were remarkably consistent during the campaign (Table 2). We have already noted that the lidar ratio was nearly constant within the two time regimes (separated by yearday 118.9) and within the two RH ranges (separated by 50% RH). This also held true for ω and $\mathring{a}$ (450 and 700, respectively). In fact, the variability was low enough that much of the measured variability can be accounted for by instrumental noise (see "SD_{meas}/noise" in Table 2). We can therefore only place an upper bound on the true variation in these parameters, and even this upper bound is quite small.

5. Comparison of measured and modeled lidar ratio

In the absence of a way to directly determine the lidar ratio, some lidar users have employed Mie theory and either measured or assumed size distributions to predict the lidar ratio. Here we have directly measured the lidar ratio of ambient aerosol and we have available size distributions that can be combined with Mie theory to predict the lidar ratio. Because the aerosol during SEAS was sea-salt dominated and because the ambient relative humidity was always above the sea-salt deliquescence point, Mie theory, which is based on an assumption of aerosol sphericity, should be able to be used to accurately predict the SEAS aerosol optical properties. This experiment thus provides a good opportunity to test for closure between measured and modeled values of the lidar ratio. As discussed above, we base our assumption that the aerosol measured by our instruments was spherical on the fact that we reach closure between the measured and Mie-calculated values of the hemispheric-backscatter fraction, $\sigma_{\text{bsp}}/\sigma_{\text{sp}}$ (see discussion below).

TABLE 2. An analysis of the mean, uncertainty, and variability of the aerosol extensive and intensive properties during SEAS. Where the ratio of the measured std dev (SD_{meas}) to instrumental noise is <2, SD_{meas} is likely to be dominated by noise and thus represents an upper limit on the true, ambient variability. In these cases, SD_{meas} is shown in parentheses. All parameters other then σ_{ap} are referenced to the RH shown in the table; σ_{ap} was derived at low RH and this value was used to calculate ω. All variables except $\mathring{a}$ are given at 532 nm.

Airmass category	All	Day < 118.9, RH_{180} > 50%	Day < 118.9, RH_{180} < 50%	Day > 118.9, RH_{180} > 50%	Day > 118.9, RH_{180} < 50%
No. 10-min samples	1106	781	34	252	39
Cut size (μm)	10	10	10	10	10
RH (%)					
Mean	64.7	67.8	42.7	60.3	42.0
SD_{meas}	8.4	5.4	5.0	5.0	4.1
			Extensive parameters		
σ_{sp} $(Mm)^{-1}$					
Mean	38.14	39.43	20.35	37.53	31.74
Uncertainty	3.76	4.00	2.09	3.37	2.91
Prec. uncertainty	0.45	0.47	0.36	0.40	0.60
SD_{meas}	10.41	9.80	4.16	10.05	7.03
SD_{meas}/noise	18.5	17.2	9.0	19.1	13.3
σ_{ap} $(Mm)^{-1}$					
Mean	0.24	0.14	0.14	0.48	0.71
Uncertainty	0.03	0.02	0.07	0.05	0.10
Prec. uncertainty	0.71	0.71	0.71	0.71	0.71
SD_{meas}	(0.39)	(0.37)	(0.26)	(0.32)	(0.33)
SD_{meas}/noise	0.5	0.5	0.3	0.4	0.4
β_p $(Mm\ sr)^{-1}$					
Mean	1.51	1.56	1.46	1.39	1.50
Uncertainty	0.15	0.14	0.17	0.18	0.23
Prec. uncertainty	0.06	0.04	0.08	0.11	0.11
SD_{meas}	0.42	0.37	0.25	0.52	0.55
SD_{meas}/noise	3.7	3.3	2.1	4.6	4.5
			Intensive parameters		
$\mathring{a}$ (450/700)					
Mean	0.07	0.03	−0.02	0.21	0.19
Uncertainty	0.38	0.37	0.38	0.37	0.38
Prec. uncertainty	0.06	0.06	0.09	0.08	0.10
SD_{meas}	(0.14)	(0.12)	(0.11)	(0.10)	(0.08)
SD_{meas}/noise	1.9	1.7	0.9	1.4	1.0
ω					
Mean	0.994	0.996	0.994	0.985	0.972
Uncertainty	0.002	0.001	0.004	0.003	0.005
Prec. uncertainty	0.026	0.025	0.046	0.025	0.029
SD_{meas}	(0.016)	(0.016)	(0.013)	(0.012)	(0.024)
SD_{meas}/noise	0.6	0.6	0.3	0.5	0.8
S					
Mean	25.7	25.4	14.3	28.2	24.7
Uncertainty	3.81	3.46	2.30	4.80	5.88
Prec. uncertainty	2.33	1.50	1.11	4.90	3.31
SD_{meas}	(3.71)	(1.76)	3.58	(3.22)	9.84
SD_{meas}/noise	1.07	0.53	2.48	0.74	3.99

The size distribution data used here were from measurements made by UH and are described in detail by Clarke et al. (2003). These size distributions have been adjusted to a relative humidity that matches that in the 180°-backscatter nephelometer using growth factors consistent with a clean marine aerosol, as described by Clarke et al. (2003). Every hour, size measurements were made for 20 min from the same height on the tower as the University of Washington optical measurements (~10 m height; UH tower location ''t2''). The size data used here thus consist of 20-min averages obtained once per hour.

We have noted that the aerosol optical properties were relatively invariant during the campaign within the two time periods before and after yearday 118.9, characterized respectively as ''clean marine'' and ''volcanically influenced.'' Here we will only test for closure between the size and optical data from the clean marine period.

For this closure study we calculated the lidar ratio and the hemispheric-backscatter fraction from the size distributions using two approaches. First, we used lognormal size distributions to approximate the measured accumulation and coarse modes (Fig. 5) such that the number (N) distribution is given by

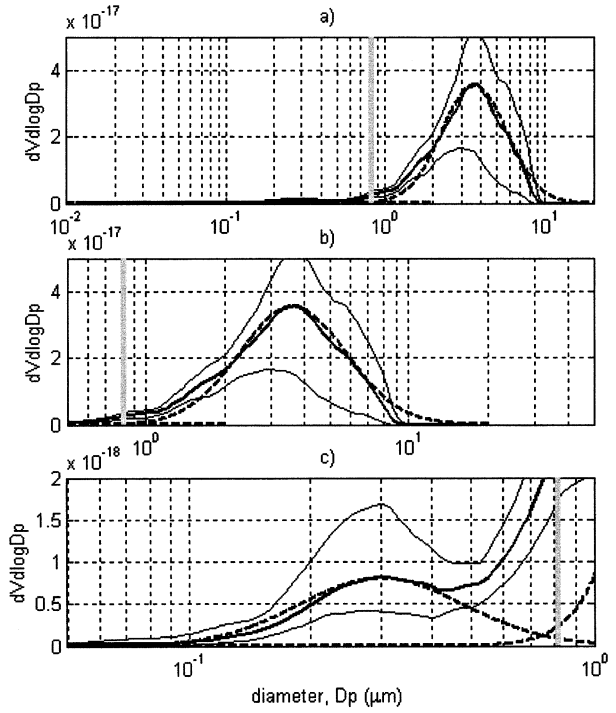

FIG. 5. The volume size distribution vs geometric diameter D_p for the clean marine case as measured (thick solid lines) and as approximated with lognormal size distributions (dashed lines). The thin lines show the range (std dev) of the size distributions during the clean marine period. Also shown is the cut point of the impactor we used for the optical measurements (vertical gray line). All three panels show the same data, but we focus on the coarse mode in (b) and on the accumulation mode in (c). Note that a significant portion (~55%) of the volume below $D_p = 0.82$ μm is due to the tail of the coarse mode.

$$\frac{dN}{d\,\ln(r)} = \frac{N}{\ln(\mathrm{Sg})\sqrt{2\pi}} \exp\left\{-\frac{[\ln(r) - \ln(r_{g0})]^2}{2[\ln(\mathrm{Sg})]^2}\right\}, \quad (14)$$

where the geometric volume mean diameter, D_{gv}, is related to the number mean radius, r_{g0}, by $D_{gv} = 2r_{g0} \exp[3 \ln(\mathrm{Sg})^2]$. The width of the size distribution is determined by the geometric standard deviation, Sg, which is set to 1.6 throughout. Volume hemispheric-backscattering, total-scattering, absorption, and 180°-backscattering efficiencies were calculated for lognormal accumulation and coarse modes using Mie theory. These efficiencies were then weighted by the relative volumes of the aerosol within each mode, which we calculated as the total aerosol volume in the measured size distributions below (accumulation mode) and above (coarse mode) 0.82-μm diameter. The lidar ratio is calculated directly as the volume-weighted extinction efficiency divided by the volume-weighted 180°-backscatter efficiency. The hemispheric-backscatter ratio is calculated in an analogous manner. As a test of the sensitivity of the lidar ratio to aerosol index of refraction we ran these simulations for real indices of refraction of $m_R = 1.35$, 1.40, and 1.45, where $m_R = 1.40$ is expected to most accurately reflect the hydrated sea-salt aerosol for the range in RH measured during SEAS (Tang and Munkelwitz 1993; Stelson 1990). There was a light-absorbing component to the submicron aerosol but not to the supermicron aerosol (cf. σ_{ap} in Tables 2 and 3). Thus, the imaginary index of refraction k was set to 0.000 for the coarse mode, and for the accumulation mode we ran simulations for $k = 0.000$ as well as for $k = 0.002$ through $k = 0.009$. This allowed us to test the sensitivity of S to single-scatter albedo and to determine the appropriate value of k for the SEAS aerosol. The value of k used for the accumulation mode was selected by matching ω of the simulated submicron aerosol (Table 4) to our measured value of ω the submicron aerosol (Table 3), yielding $k = 0.006$.

Finally, we tested the sensitivity of S to the volume

TABLE 3. Optical properties for aerosol of geometric diameter $D < 0.82$ μm during SEAS. Means are separately shown for the clean marine aerosol (yearday < 118.9 UTC) and the volcanically influenced aerosol (yearday > 118.9 UTC). All values except $\mathring{a}$ are given at 532 nm.

Air mass	All	yearday < 118.9, $RH_{180} > 50\%$	yearday > 118.9, $RH_{180} > 50\%$
No. 1-min data points	1396	917	479
σ_{sp} $(Mm)^{-1}$	5.64	5.03	6.82
σ_{ap} $(Mm)^{-1}$	0.28	0.20	1.45
β_p $(Mm\ sr)^{-1}$	0.098	0.087	0.120
$\mathring{a}$ (450/700)	1.94	1.95	1.94
ω	0.953	0.965	0.939
S (sr)	60.5	60.1	60.6

TABLE 4. The lidar ratio for aerosol of geometric diameter $D_p < 0.82$ μm only, as derived using only the accumulation-mode distribution (accumulation mode only) and as derived using both the accumulation-mode distribution and the tail of the coarse-mode distribution that falls below 0.82 μm (accumulation + coarse-mode tail; see Fig. 5). The data in the latter category simulate our optical measurements of the lidar ratio, assuming our submicron impactor has a perfect cutoff at $D = 0.82$ μm. The modeled ω matches that measured for the clean marine case when $m_R = 1.400$ and $k = 0.006$ (boldface). Unfortunately, a significant portion of the volume in the $D < 0.82$ μm aerosol is due to the tail of the coarse mode. If our impactor cutoff is at a smaller aerosol diameter than we think or if the cutoff is not perfectly sharp, then the portion of the scattering due to aerosols near the cut size will increase or decrease dramatically. Therefore, we have shown the lidar ratio for the accumulation-mode aerosol only as a test of how sensitive the derived value of S is the inclusion of the coarse-mode tail.

		Accumulation mode only		Accumulation + coarse-mode tail	
m_R	k	ω	S	ω	S
1.350	0.000	1.000	63.5 sr	1.000	69.7 sr
1.400	0.000	1.000	61.2 sr	1.000	64.4 sr
1.450	0.000	1.000	59.3 sr	1.000	60.1 sr
1.400	0.002	0.984	62.8 sr	0.988	65.6 sr
1.400	0.003	0.976	63.7 sr	0.982	66.4 sr
1.400	0.004	0.969	64.5 sr	0.977	67.0 sr
1.400	0.005	0.961	65.4 sr	0.971	67.7 sr
1.400	0.006	0.953	66.2 sr	**0.965**	**68.3 sr**
1.400	0.007	0.946	67.1 sr	0.960	69.0 sr
1.400	0.008	0.939	67.9 sr	0.954	69.6 sr
1.400	0.009	0.932	68.8 sr	0.949	70.3 sr

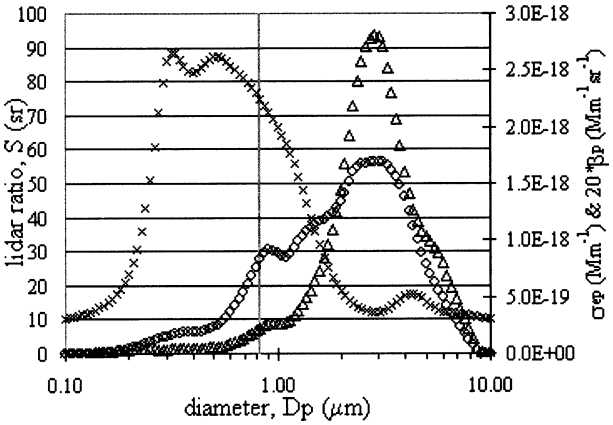

FIG. 6. The lidar ratio (crosses), light extinction (circles), and 180° backscatter (triangles; multiplied by 20 for ease of plotting) as calculated at a function of geometric diameter D_p for the size distributions shown in Fig. 5. Data shown are for the clean marine case using lognormal size distributions [Eq. (15)] with Sg = 1.2 and $m = 1.400 + 0.00i$. Also shown is the nominal cut point ($D_p = 0.82$ μm) of the submicron impactor used in our optical measurements (gray line).

mean geometric diameters, D_{gv}, of the accumulation- and coarse-mode lognormal size distributions by running the simulation for three values of D_{gv}: 1) $D_{gv,best}$, which is the diameter of the peak in the measured volume size distribution (Fig. 5); 2) $D_{gv,min} = D_{gv,best} - \Delta D_{gv}$; and 3) $D_{gv,max} = D_{gv,best} + \Delta D_{gv}$. For the coarse mode, $D_{gv,best}$ and ΔD_{gv} are 0.30 and 0.05 μm, respectively, and for the accumulation mode they are 3.63 and 0.34 μm.

In a second set of simulations we directly used the size data to calculate the optical properties of the aerosol within each size bin. The lidar ratio of the total aerosol was then calculated by weighting each bin's extinction and 180°-backscatter efficiencies by the volume of aerosol within that bin. The hemispheric-backscatter fraction was calculated in an analogous manner. Figure 6 shows how different regions of the particle size spectrum contribute to the calculated value of the lidar ratio when $m_R = 1.400$ and $k = 0.000$.

To simulate our submicron aerosol measurements, we assumed a particle density of 1.5 g cm^{-3}, such that the $D_{aero} = 1$ μm cut size of our impactor corresponds to a geometric diameter of $D_p = 0.82$ μm. Simulations were run using the same two approaches described above but only including scattering and absorption from aerosol of diameter $D_p < 0.82$ μm (Tables 4, 5).

Discussion of closure study results

Using the two methods described above to represent the SEAS aerosol, we found that the modeled values of the lidar ratio were somewhat lower than the optically measured values for the total aerosol and were somewhat higher than the measured values for the submicron aerosol, as summarized below.

TABLE 5. The lidar ratio of the total and submicron aerosol, as derived using two lognormal size distributions to simulate the measured accumulation and coarse modes. Results are shown for a range of real indices of refraction, m_R, and geometric mean diameters, D_{gv}. The imaginary index of refraction k is fixed at 0.000 for the coarse mode and 0.003 for the accumulation mode. The ratio of coarse-mode volume to accumulation-mode volume is 44:1 for the total aerosol. The extinction and 180°-backscattering efficiencies used to calculate S are weighted accordingly. The overall best guess values for the total and submicron modeled values of S are shown in bold.

Total aerosol	D_{gv} of the accumulation mode	D_{gv} of the coarse mode	Total aerosol lidar ratio S
$m_R = 1.350$	0.30 μm	3.29 μm	18.98 sr
		3.63 μm	18.47 sr
		3.97 μm	18.32 sr
$m_R = 1.400$	0.30 μm	3.29 μm	16.89 sr
		3.63 μm	**16.51 sr**
		3.97 μm	16.26 sr
$m_R = 1.450$	0.30 μm	3.29 μm	16.85 sr
		3.63 μm	16.72 sr
		3.97 μm	16.63 sr
Submicron aerosol	D_{gv} of the accumulation mode	D_{gv} of the coarse mode	Submicron aerosol lidar ratio S
$m_R = 1.400$	0.25 μm	3.63 μm	58.9 sr
	0.30 μm		**68.3 sr**
	0.35 μm		74.3 sr

Lidar ratio, all aerosol	
Optically measured	25.4 + 3.5 sr
Model method 1, lognormal distributions	16.5 sr
Model method 2, direct size data	20.3 sr
Lidar ratio, submicron aerosol	
Optically measured	68 ± 10 sr
Model method 1, lognormal distributions	66.4 sr
Model method 2, direct size data	74.4 sr

The errors in both cases are ~20% and ~10% for the total and submicron aerosol, respectively (comparing measured versus the more exact model method 2), while the uncertainty in the measured values is ~15%. We do not attempt to quantify the uncertainties in the model values but show sensitivities in the modeled values of S to its controlling parameters (Tables 4, 5). These tests show that it would be difficult to reach agreement between the modeled and measured values of S for the total aerosol because S is not very sensitive to modest changes in refractive index and size (Table 5). However, small errors in the accumulation-mode size could readily explain the differences between the measured and modeled values of S for the submicron aerosol (Table 5). The lack of closure for S for the total aerosol could be either 1) because the aerosol measured by the optical instruments is in fact considerably smaller than that given by the size distributions, which include substantial inlet efficiency corrections (Clarke et al. 2003) or 2) due to nonspherical

effects, which could bias the angular corrections factor for β_p and the size-derived optical properties.

In contrast, we found agreement between the measured and modeled hemispheric-backscatter fraction, within the uncertainty of the optical measurements.

Hemispheric-backscatter fraction, all aerosol:

Optically measured	0.083 ± 0.016
Model method 2, direct size data	0.075

In this modeling effort, we have tried to bound uncertainties in our size-derived optical properties by varying the input parameters D_{gv}, m_R, and k in our Mie calculations based on lognormal distributions (model method 1). The results of these tests tell us something about the sensitivity of S to changes in these parameters and give us insight as to what parameters must be well known in order to accurately predict S. From these tests, we see that the sensitivity of S to changes in one parameter depends in part on the value of the other two parameters. For example, S appears to be more sensitive to changes in D_{gv} for the accumulation-mode aerosol than for the coarse-mode aerosol (Table 5). The reason for this is revealed by looking at how S varies with aerosol size (Fig. 6); the accumulation-mode aerosol is centered at $D_{gv} = 0.30$ μm, where there is a large gradient in S versus D_{gv}. In contrast, the coarse-mode aerosol is centered on $D_{gv} = 3.6$ μm, where S is relatively invariant with D_{gv}. Inspection of Fig. 6 also reveals why the lidar ratio of all aerosol with $D_p < 0.82$ μm (accumulation mode plus the lower tail of coarse mode) is higher than S of the accumulation mode alone: the lower tail of the coarse mode falls within the size range (~0.6–0.8 μm), where S is high.

The size-derived values of S for the submicron aerosol will also be sensitive to errors in the diameter and shape of the impactor cut point we have used in the model. We have assumed that the impactor transmission goes from 100% to 0% at 0.82 μm, when in fact the transmission function is more likely a steep change in transmission between ~0.77 and ~0.87 μm (Hillamo and Kauppinen 1991). Between 0.7 and 0.9 μm S decreases with size, while the contribution to extinction increases with size (Fig. 6). Thus, the assumption of a perfect impactor cut point may be leading to a slight overestimation in our model-derived S for submicron aerosol. On the other hand, error in the central cut point of the impactor could be leading to either a positive or negative error in S (Fig. 6).

As an additional test of the measured and modeled optical properties, we compared the fine-mode fraction (FMF) of light scattering (FMF_{scat}) and the Ångström exponent. FMF_{scat} was derived using the optical instruments and an 0.82-μm cut size impactor and was modeled using method 2 described above, with aerosol concentrations set to zero for diameters $D > 0.82$ μm. The size distributions and Mie theory (modeling method 2) give a fine-mode fraction of 14.2%, which agrees well with the optically derived FMF_{scat} of 15.4 ± 3.5%. For the Ångström exponent we get measured values of $\mathring{a} = 0.03 \pm 0.12$, versus a modeled value of −0.02. However, the uncertainty in the measured values is 0.37, so the two do agree to within the measurement uncertainty.

6. Conclusions

We have presented the results from measurements of aerosol optical properties at a coastal marine site on the island of Oahu, Hawaii, from 16 April to 1 May 2000. The goal of these measurements was to empirically determine the lidar ratio for sea-salt-dominated aerosol. These data comprise the first robust in situ measurements of coarse-mode-dominated aerosol with the 180°-backscatter nephelometer. During SEAS, we measured the lidar ratio at 532 nm to be 25.4 ± 1.8 sr (mean ± standard deviation), with a 95% CI uncertainty in this mean of 3.5 sr. The sampled air consisted of a background marine aerosol periodically supplemented by aerosol from wave breaking at an offshore reef and at the beach next to the measurement tower. Clarke et al. (2003) show that only about 10% of the scattering at our sample inlet was attributable to aerosol from breaking waves. The consistency in the lidar ratio across the measurement period implies that there was little sensitivity in S to the presence of this wave-break aerosol, which was modulated by both the tide height and winds. Thus the measured value of $S = 25 \pm 4$ sr should be applicable for general open-ocean conditions.

The SEAS measurements also provided a test of the Bond et al. (1999) scattering correction to PSAP measurements of light absorption for the case of coarse-mode aerosol. Using a low flow rate (1 L m^{-1}) and correcting σ_{ap} with nephelometer-measured scattering (i.e., no angular correction), we have shown that the 2% scattering correction is not too large for aerosol dominated by a conservatively scattering coarse mode.

The campaign had two distinct periods: clean marine before yearday 118.9 UTC (~2130 UTC April 27) and volcanically influenced marine after yearday 118.9 (Table 2). The aerosol optical properties throughout the campaign were dominated by coarse-mode sea salt, but an accumulation mode of unknown composition was also present during both periods. The change from ''clean marine'' to ''volcanically influenced'' was manifested as an increase in the volume concentration of the accumulation-mode aerosol (Clarke and Kapustin 2003), a decrease in the accumulation-mode single-scatter albedo (Table 3), and an increase the lidar ratio (Table 2). While aerosol concentrations varied widely, the intensive aerosol characteristics (ω, $\mathring{a}$, and S) were extremely consistent within the two time periods, as long as the measurement RH was greater than 50%. In comparison to a polluted continental site, the SEAS aerosol optical properties were both less variable and less temporally coherent (Fig. 4).

The most dramatic change in the SEAS aerosol optical properties was a drop in the lidar ratio when we intentionally heated the sample air, driving the RH to below

50% (Table 2). We attribute the shift in S at 50% RH to a change in aerosol morphology, as the crystallization point for sea salt is ~47% RH.

Using size distributions we were able to do a closure study between our empirically derived values of the lidar ratio and the same as determined using Mie theory. Comparisons were made for the clean marine period both for the total and submicron aerosol, but only for times when the nephelometer sample RH was greater than 50%. Using a value of m_R that is appropriate for sea salt and values of k that were set by matching the measured and modeled values of ω, we found that the size-derived values of S for the total aerosol were ~20% lower than those measured optically. However, agreement well within the uncertainty of the optical measurements was reached between the measured and modeled values of the hemispheric-backscatter fraction, in contrast to previous studies where sea-salt aerosol was measured below the crystallization point (Quinn et al. 1995, 1996). The reason for lack of closure with S is unclear, but it may be due to shape effects or sizing errors that affect the lidar ratio more than hemispheric-backscatter fraction.

Sensitivity tests of the modeled value of S to changes in m_R, k, and D_{gv} were performed. For accumulation-mode aerosol, small uncertainties in D_{gv} and m_R yield large variations in S (Tables 4 and 5). Coarse-mode-dominated aerosol, on the other hand, is less sensitive to changes in D_{gv} and m_R (Table 5). These tests give us some indication of when lidar operators should be cautious about using values of S derived from measured or assumed size distributions and indices of refraction.

The results presented herein apply to sub-10-μm marine aerosol measured near the surface. Vertically resolved measurements are needed to determine the generality of these results to the entire marine boundary layer.

Acknowledgments. The work described herein was funded by the Office of Naval Research under Grant N00014-98-1-0809. This publication is partially supported by a grant to the Joint Institute for the Study of the Atmosphere and Ocean (JISAO) under NOAA Cooperate Agreement NA17RJ1232.

REFERENCES

Ackermann, J., 1998: The extinction-to-backscatter ratio of tropospheric aerosol: A numerical study. *J. Atmos. Oceanic Technol.,* **15,** 1043–1050.

Anderson, T. L., and J. A. Ogren, 1998: Determining aerosol radiative properties using the TSI 3563 integrating nephelometer. *Aerosol Sci. Technol.,* **29,** 57–69.

——, and Coauthors, 1996: Performance characteristics of a high-sensitivity, three-wavelength, total scatter/backscatter nephelometer. *J. Atmos. Oceanic Technol.,* **13,** 967–986.

——, S. J. Masonis, D. S. Covert, R. J. Charlson, and M. J. Rood, 2000: In situ measurements of the aerosol extinction-to-backscatter ratio at a polluted continental site. *J. Geophys. Res.,* **105,** 26 907–26 915.

Ansmann, A., M. Riebesell, and C. Weitkamp, 1990: Measurement of atmospheric aerosol extinction profiles with a Raman lidar. *Opt. Lett.,* **15,** 746–748.

——, ——, U. Wandinger, C. Weitkamp, E. Voss, W. Lahmann, and W. Michaelis, 1992: Combined Raman elastic-backscatter LIDAR for vertical profiling of moisture, aerosol extinction, backscatter, and LIDAR ratio. *Appl. Phys.,* **55B,** 18–28.

Bond, T. C., T. L. Anderson, and D. Campbell, 1999: Calibration and intercomparison of filter-based measurements of visible light absorption by aerosols. *Aerosol Sci. Technol.,* **30,** 582–600.

Carrico, C. M., M. J. Rood, and J. A. Ogren, 1998: Aerosol light scattering properties at Cape Grim, Tasmania, during the First Aerosol Characterization Experiment (ACE 1). *J. Geophys. Res.,* **103,** 16 586–16 574.

——, ——, ——, C. Neusüß, A. Wiedensohler, and J. Heintzenberg, 2000: Aerosol optical properties at Sagres, Portugal during ACE-2. *Tellus,* **52B,** 694–715.

Clarke, A., and V. Kapustin, 2003: The Shoreline Environment Aerosol Study (SEAS): A context for marine aerosol measurements influenced by a coastal environment and long-range transport. *J. Atmos. Oceanic Technol.,* **20,** 1351–1361.

——, ——, ——, ——, ——, S. Masonis, T. Anderson, and D. Covert, 2003: Sea-salt size distributions from breaking waves: Implications for marine aerosol production and optical extinction measurements during SEAS. *J. Atmos. Oceanic Technol.,* **20,** 1362–1374.

Covert, D. S., R. J. Charlson, and N. C. Ahlquist, 1972: A study of the relationship of chemical composition and humidity to light scattering by aerosols. *J. Appl. Meteor.,* **11,** 968–976.

Doherty, S. J., T. L. Anderson, and R. J. Charlson, 1999: Measurement of the lidar ratio for atmospheric aerosols using a 180° backscatter nephelometer. *Appl. Opt.,* **38,** 1823–1832.

Ferrare, R. A., S. H. Melfi, D. N. Whiteman, K. D. Evans, and R. Leifer, 1998a: Raman lidar measurements of aerosol extinction and backscattering: 1. Methods and comparisons. *J. Geophys. Res.,* **103,** 19 663–19 672.

——, ——, ——, ——, M. Poellot, and Y. J. Kaufman, 1998b: Raman lidar measurements of aerosol extinction and backscattering: 2. Derivation of aerosol real refractive index, single-scattering albedo, and humidification factor using Raman lidar and aircraft size distribution measurements. *J. Geophys. Res.,* **103,** 19 673–19 689.

Foot, J. S., and C. G. Kilsby, 1989: Absorption of light by aerosol particles: An intercomparison of techniques and spectral observations. *Atmos. Environ.,* **23,** 489–495.

Gasso, S., and Coauthors, 2000: Influence of humidity on the aerosol scattering coefficient and its effect on the upwelling radiance during ACE-2. *Tellus,* **52B,** 546–567.

Grund, C. J., and E. W. Eloranta, 1991: University of Wisconsin high spectral resolution lidar. *Opt. Eng.,* **30,** 6–12.

Hillamo, R. E., and E. I. Kauppinen, 1991: On the performance of the Berner low pressure impactor. *Aerosol Sci. Technol.,* **14,** 33–47.

Kotchenruther, R. A., P. V. Hobbs, and D. A. Hegg, 1999: Humidification factors for atmospheric aerosols off the mid-Atlantic coast of the United States. *J. Geophys. Res.,* **104,** 2239–2251.

Masonis, S. J., K. Franke, A. Ansmann, D. Mueller, D. Althausen, J. A. Ogren, A. Jefferson, and P. J. Sheridan, 2002: An intercomparison of aerosol light extinction and 180° backscatter as derived using in-situ instruments and Raman lidar during the INDOEX field campaign. *J. Geophys. Res.,* **107,** 8014, doi:10.1029/2000DJ000035.

Mattis, I., A. Ansmann, D. Muller, U. Wandinger, and D. Althausen, 2002: Dual-wavelength Raman lidar observations of the extinction-to-backscatter ratio of Saharan dust. *Geophys. Res. Lett.,* **29,** 1306, doi:10.1029/2002GL014721.

Mishchenko, M. I., L. D. Travis, R. A. Kahn, and R. A. West, 1997: Modeling phase functions for dustlike tropospheric aerosols using a shape mixture of randomly oriented polydisperse spheroids. *J. Geophys. Res.,* **102,** 16 831–16 847.

Piironen, P., and E. W. Eloranta, 1994: Demonstration of a high-spectral-resolution lidar based on an iodine absorption filter. *Opt. Lett.,* **19,** 234–236.

Quinn, P. K., S. Marshall, T. S. Bates, D. S. Covert, and V. N. Kapustin,

1995: Comparison of measured and calculated aerosol properties relevant to the direct radiative forcing of tropospheric sulfate aerosol on climate. *J. Geophys. Res.*, **100,** 8977–8991.

——, and Coauthors, 1996: Closure in tropospheric aerosol-climate research: A review and future needs for addressing aerosol direct shortwave radiative forcing. *Beitr. Phys. Atmos.*, **69,** 547–577.

Reagan, J. A., J. D. Spinhirne, D. M. Byrne, D. W. Thomson, R. G. De Pena, and Y. Mamane, 1977: Atmospheric particulate properties inferred from lidar and solar radiometer observations compared with simultaneous in situ aircraft measurements: A case study. *J. Appl. Meteor.*, **16,** 911–928.

Shipley, S. T., D. H. Tracy, E. W. Eloranta, J. T. Trauger, J. T. Sroga, F. L. Roesler, and J. A. Weinman, 1983: High spectral resolution lidar to measure optical scattering properties of atmospheric aerosols. 1: Theory and instrumentation. *Appl. Opt.*, **22,** 3716–3724.

Spinhirne, J. D., J. A. Reagan, and B. M. Herman, 1980: Vertical distribution of aerosol extinction cross section and inference of aerosol imaginary index in the troposphere by lidar technique. *J. Appl. Meteor.*, **19,** 426–438.

Sroga, J. T., E. W. Eloranta, S. T. Shipley, F. L. Roesler, and P. J. Tryon, 1983: High spectral resolution lidar to measure optical scattering properties of atmospheric aerosols. 2: Calibration and data analysis. *Appl. Opt.*, **22,** 3725–3732.

Stelson, A. W., 1990: Urban aerosol refractive indices prediction by partial molar refraction approach. *Environ. Sci. Technol.*, **24,** 1676–1679.

Tang, I. N., and H. R. Munkelwitz, 1993: Composition and temperature dependence of the deliquescence properties of hygroscopic aerosols. *Atmos. Environ.*, **27A,** 467–473.

——, A. C. Tridico, and K. H. Fung, 1997: Thermodynamic and optical properties of sea salt aerosols. *J. Geophys. Res.*, **102,** 23 269–23 275.